

Estimating energy input rate from vertical profiles of energy dissipation rate

Nozomi Sugiura¹, Shinya Kouketsu¹, Shuhei Masuda¹, Satoshi Osafune¹, and Ichiro Yasuda²

¹Research and Development Center for Global Change, JAMSTEC, Yokosuka, Japan

²Atmosphere and Ocean Research Institute, University of Tokyo, Chiba, Japan

Correspondence to: Nozomi Sugiura (nsugiura@jamstec.go.jp)

Abstract. The energy dissipation rate is an important characteristic of turbulence; however, its magnitude in observational profiles can be misidentified owing to its erratic evolution. By analyzing observed data from oceanic turbulence, we show that the vertical sequences of depth-averaged energy dissipation rates have a scaling property. We propose a method to estimate the energy input rate by utilizing this property. It is found that for scaling in the observed profiles, our data have a statistical property consistent with the universal multifractal model, which comprises α -stable generators with parameters $\alpha = 1.63$ and $C_1 = 0.373$. This determines the averaging rule of the energy dissipation rates in the logarithmic space. Meanwhile, the energy input rate and its uncertainty can be estimated by assimilating vertical profile data into the cascade model, which serves as an alternative to the arithmetic average over the vertical data sequence.

1 Introduction

The importance of determining the energy dissipation rate to study ocean general circulation has been highlighted in numerous studies (e.g. Gregg et al., 1973; Munk and Wunsch, 1998). Hence, a large number of observational studies have been conducted to obtain the vertical profiles of the energy dissipation rate using ocean microstructure profilers (e.g., Waterhouse et al., 2014; Waterhouse and McKinnon, 2014). In addition, to understand the statistics of the erratic evolution of observational profiles, studies have been conducted from the viewpoint of statistical fluid mechanics, as summarized below.

In fully developed turbulence, there exists an inertial subrange where the advective term is dominant over the molecular viscosity term in the Navier–Stokes equation (e.g., Pope, 2000). In the inertial subrange, there is a cascade of energy from large to small, as intuitively stated by (e.g., Richardson, 1922). As the first quantitative theory on the energy cascade, Kolmogorov (1941) established a relationship wherein velocity fluctuations are locally isotropic and are determined by the homogeneous energy dissipation rate,

$$\langle |v(x + \ell) - v(x)| \rangle \approx \epsilon^{1/3} \ell^{1/3}, \quad (1)$$

where $\langle \cdot \rangle$ denotes the ensemble average. Subsequently, it was criticized that the energy dissipation rate is not homogeneous but shows significant random fluctuations (Landau and Lifshitz, 1987). A refined theory was proposed to address this issue (Kolmogorov, 1962). The theory stated that i) $\log \epsilon_r$, which is the logarithm of the spatially averaged energy dissipation rate over scale r , obeys a Gaussian distribution, and ii) its variance obeys $\sigma_{\log \epsilon_r}^2 = A + \mu \log(L/r)$ (L : the outer scale).

Additionally, several experimental studies (Gurvich and Zubkovskii, 1963; Pond and Stewart, 1965) showed that small-scale dissipation is a random field that has a spatial structure with power-law correlations,

$$\langle \epsilon(x)\epsilon(x + \ell) \rangle \propto \ell^{-\mu}. \quad (2)$$

Then, Yaglom (1966) formulated a quantitative model, which was consistent with the scaling log-normality and the power-law correlations, as a multiplicative cascade, where ϵ_r was expressed with a binary tree composed of i.i.d random variables, $W_{i,k} (\sim W)$,

$$\forall 1 \leq j \leq 2^n, \quad \epsilon_r(x_j) = \prod_{i=1}^n W_{i,[(j-1)/2^{n-i}]+1}, \quad (3)$$

where $[\cdot]$ is the Gauss symbol. If the random variables are set to have the moment exponent, $K(q) = \log_2 \langle W^q \rangle = (\mu/2)(q^2 - q)$, then the energy conservation and the log-normality at each scale in Kolmogorov (1962) are reproduced. Moreover, correlation (2) is reproduced because we have $\langle \epsilon(x)\epsilon(x + \ell) \rangle = \langle W^2 \rangle^{n-m} \langle W \rangle^{2m} \propto \ell^{-K(2)}$, where $L = 2^n r$, $\ell = 2^m r$ for small r (Yaglom, 1966; Monin and Yaglom, 2013).

There have been several alternative multiplicative cascade models with different generators, including the β -model (Frisch et al., 1978), random β -model (Benzi et al., 1984), α -model (Schertzer and Lovejoy, 1984), p -model (Meneveau and Sreenivasan, 1987), log-stable model (Schertzer and Lovejoy, 1987), and log-Poisson model (She and Leveque, 1994). An important observation regarding Yaglom's cascade is that the property required for the law of random variable W can be abstracted such that the product of several random variables still obeys the same class of distribution, $\prod_{i=1}^n W_i \sim a_n W^{b_n}$, with $a_n, b_n > 0$ (e.g., Schmitt and Huang, 2016). Consistent with this condition, the universal multifractal model (Schertzer and Lovejoy, 1987) employs a stable Lévy generator, Γ , that is maximally left skewed, and $W = e^\Gamma$ is set. This results in a simple and nonanalytic form of the moment exponent, $K(q) = (C_1/(\alpha - 1))(q^\alpha - q)$. The universal multifractal model is the most promising model. It can be used to model the variability in several phenomena including turbulence, other geophysical phenomena, and several fractal-like appearances in natural objects and even man-made objects.

Based on this theory, we reconsider one of the basic questions in the observational study of ocean turbulence: how can one estimate energy intensity, or the energy input rate, from the vertical profile data of the energy dissipation rate, which has been commonly equated with the arithmetic mean over the profile. Our question pertains to whether one can obtain information regarding energy intensity beyond the arithmetic average. The answer is yes because we can construct a model for the turbulent cascade process and solve the inversion problem to obtain the energy input rate under an observational constraint. In this study, we first show that the observed profiles of the depth-averaged energy dissipation rate, ϵ_r , have a scaling property that is consistent with the universal multifractal model. Then, we construct a multiplicative cascade simulation model that describes the statistics in observational data. We propose a method to explain certain statistics of the observed profiles based on a simulation model and develop an inversion method to estimate the energy input rate. This result should provide a systematic method of gaining further quantitative information from profile data.

The remainder of this paper is organized as follows: Section 2 describes the turbulence observation data. Section 3 describes the scaling analysis of the moments to derive the moment scaling exponent within the universal multifractal framework. Sec-

tion 4 discusses the methods for estimating several quantities from observational data based on simulation and assimilation using the cascade model. Finally, section 5 concludes the paper.

2 Observational data

In this section, we describe the turbulence observational data employed in this study. The turbulence observational data were retrieved from the Pacific ocean (Fig. 1) (Goto et al., 2018), and they comprise approximately 400 profiles, each of which typically extends over a depth of 2000 to 6000 m below the sea surface, with observational points every 5 to 10 m.

The turbulent energy dissipation rates, ϵ , were estimated as follows: Microscale temperature fields were observed using the fast-response Fasttip Probe model 07 (FP07) thermistors attached to frames for measuring conductivity, temperature, and depth (CTD) as common oceanographic observational platforms. ϵ was derived by detecting the Batchelor wavenumber (Batchelor, 1959) and fitting (Ruddick et al., 2000) a theoretical spectrum (Kraichnan, 1968) to the observed temperature vertical gradient spectra after correcting the spectra with a double-pole function with a time constant of 3ms (Goto et al., 2016). Each data point was evaluated for a depth interval of approximately 10m with half overlap to yield 5dbar interval data. Herein, we included all data without any quality screening to consider the extreme values, which are important for investigating intermittency.

We estimated the turbulent energy dissipation rate from temperature measurement in each observational bin with a width of $r_0 \simeq 10\text{m}$ by utilizing a fitting method based on analytical spectral closure (see Appendix A for the estimation principle). We restricted our investigation to the intermittency occurring at larger scales, $r > r_0$.

Let r_0 be the bin width, \vec{x}_j the horizontal coordinate of the j -th profile, and z_k the vertical coordinate of the k -th point in the j -th profile. These positive-valued data have the following characteristics:

1. Each profile defines an ordered set,

$$\left\{ \epsilon_{r_0}(\vec{x}_j, z_{k_j}) \mid k_j = 1, 2, \dots, K_j \right\},$$

which exhibits an extremely erratic evolution that impedes the recognition of a continuous curve along the depth direction (Fig. 2(a)).

2. After taking the logarithm of the values, the sequences appear to be more continuous (Fig. 2(b)).
3. If we normalize each value with the arithmetic mean along the profile it belongs to, the histogram of the logarithmic values,

$$\left\{ \log \left(\frac{\epsilon_{r_0}(\vec{x}_j, z_{k_j})}{K_j^{-1} \sum_{k_j} \epsilon_{r_0}(\vec{x}_j, z_{k_j})} \right) \mid j = 1, 2, \dots, J; k_j = 1, 2, \dots, K_j \right\},$$

appears as an asymmetric distribution (cyan in Fig. 6), which is discussed below.

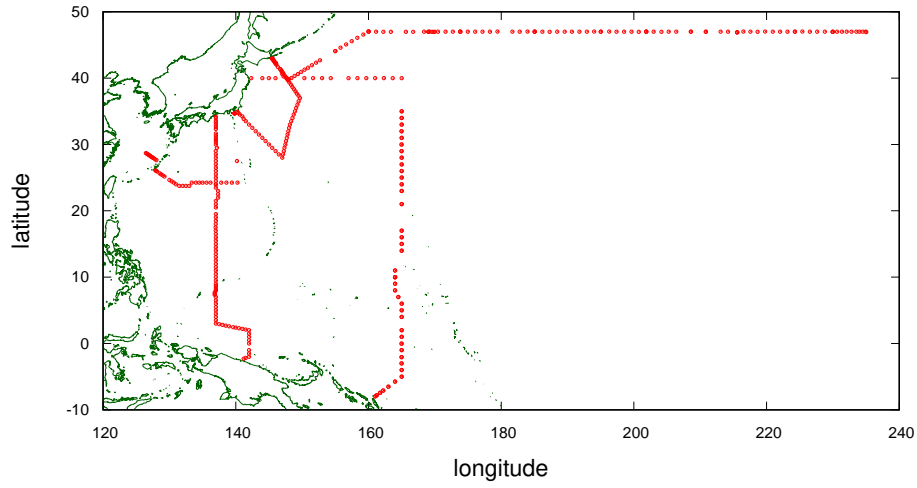


Figure 1. Horizontal locations of the observed profiles (red) and land–sea boundaries (green). The units of longitude and latitude are °E and °N, respectively.

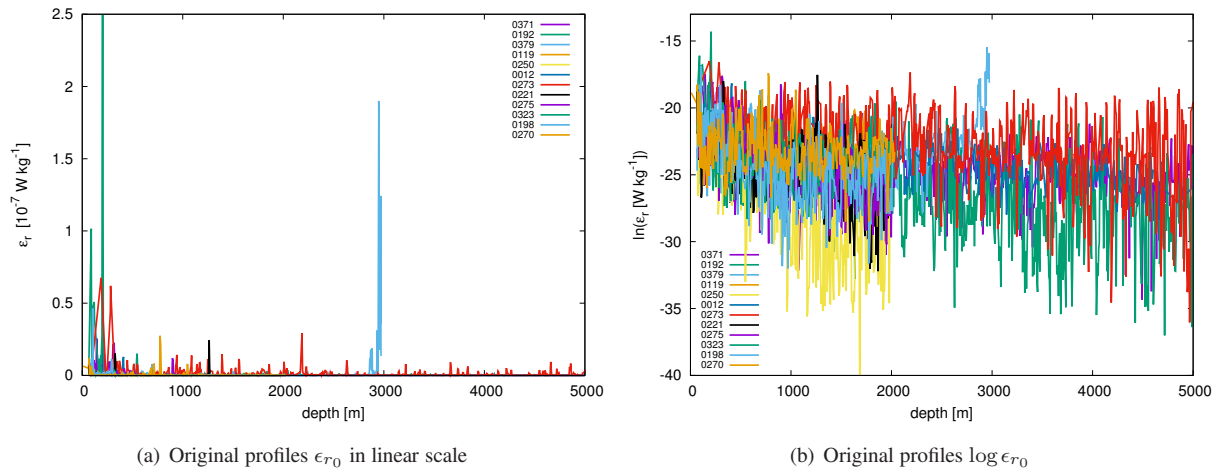


Figure 2. Appearances of observed profiles.

3 Multifractal analysis

We perform the scaling analysis of the moments to derive the moment scaling exponent within the universal multifractal framework.

3.1 Universal multifractal model

The basic formulation of the universal multifractal model is as follows (e.g., Lovejoy and Schertzer, 2013; Gires et al., 2013): Suppose we have a multifractal field, ε_λ , at resolution $\lambda (= L/r)$, where r is the observational scale and L is the outer scale. The field is normalized by the mean, $\langle \varepsilon_\lambda \rangle = \langle \varepsilon \rangle$, which is conserved at all scales.

The probability of exceeding a scale-dependent threshold, λ^γ , varies according to singularity γ as

$$Pr(\varepsilon_\lambda \geq \lambda^\gamma) \approx \lambda^{-c(\gamma)}, \quad (4)$$

where $c(\gamma)$ is the codimension function and \approx represents the equality up to the multiplication of a slowly varying function of γ . Thus, the multifractal model is characterized by the property that the codimension varies with the singularity. This relation is equivalently represented as the scaling of the statistical moment of any order, q ,

$$\langle (\varepsilon_\lambda)^q \rangle = \lambda^{K(q)}, \quad (5)$$

where $K(q)$ is the moment scaling function. The two functions, $K(q)$ and $c(\gamma)$, are actually compatible by the Legendre transformation because the moment generation function can be written in terms of the occurrence probability of singular events using the saddle-point approximation, $\langle (\varepsilon_\lambda)^q \rangle = \int \lambda^{q\gamma} dp(\gamma) \approx \lambda^{\max_\gamma \{q\gamma - c(\gamma)\}}$ (Parisi and Frish, 1985). Functions $K(q)$ and $c(\gamma)$ determine the variability of multifractal field ε_λ across the scales, λ .

Owing to a generalization of the central limit theorem, many multiplicative processes composed of different generators converge to a universal multifractal (Schertzer and Lovejoy, 1987, 1997), whose moment exponent has the following form:

$$K(q) = \frac{C_1}{\alpha - 1} (q^\alpha - q), \quad (6)$$

where $0 \leq \alpha \leq 2$ is the multifractal index and C_1 is the codimension of the mean. This also satisfies probability normalization, $K(0) = 0$, and energy conservation, $K(1) = 1$. The Legendre transformation of this gives $c(\gamma)$ in the following form:

$$c(\gamma) = C_1 \left(\frac{\gamma}{C_1 \alpha'} + \frac{1}{\alpha} \right)^{\alpha'}, \quad (7)$$

where $1/\alpha + 1/\alpha' = 1$.

3.2 Analysis of observational data

Suppose we have the observational data of the energy dissipation rate, $\varepsilon_{r_0}(\vec{x})$, in bin width r_0 at horizontal position \vec{x} and their spatial average $\varepsilon_r(\vec{x})$ in width r . In terms of these data, Eq. (5) reads

$$\frac{\langle (\varepsilon_r(\vec{x}))^q \rangle}{\langle \varepsilon(\vec{x}) \rangle^q} = \left(\frac{L}{r} \right)^{K(q)}, \quad \frac{\langle (\varepsilon_{r_0}(\vec{x}))^q \rangle}{\langle \varepsilon(\vec{x}) \rangle^q} = \left(\frac{L}{r_0} \right)^{K(q)}. \quad (8)$$

Hereafter, the normalization constant, $\langle \epsilon(\vec{x}) \rangle$, is referred to as the energy input rate, $\bar{\epsilon}(\vec{x})$, at horizontal position \vec{x} . The moment at scale r_0 is decomposed into a product as

$$\langle (\epsilon_{r_0}(\vec{x}))^q \rangle = \langle (\epsilon_r(\vec{x}))^q \rangle \langle (\epsilon_r(\vec{x})/\epsilon_{r_0}(\vec{x}))^q \rangle \quad (9)$$

because the cascade process in the scales from L to r is independent of the cascade process in the scales from r to r_0 ($L > r > r_0$). By substituting Eqs. (8) into Eq. (9), we get

$$\left\langle \left(\frac{\epsilon_r(\vec{x})}{\epsilon_{r_0}(\vec{x})} \right)^q \right\rangle = \left(\frac{r}{r_0} \right)^{-K(q)}, \quad (10)$$

for arbitrary horizontal position \vec{x} .

Based on Eq. (10), we perform a scaling analysis of observational data with respect to various moment exponents, q , by estimating the slope of the approximation straight line for the observational plots at various resolutions, r/r_0 ,

$$\left(\log(r/r_0), -\log \left\langle (\epsilon_r/\epsilon_{r_0})^{q/c} \right\rangle \right), \quad (11)$$

where the expectation is also taken across all profiles. Factor $1/c$ is required for the following reason: If the observational points in a profile are arranged with uneven spacing and their coordinates are approximated by a power function:

$$z_k = ak^c + b, \quad k = 0, 1, 2, \dots, \quad (12)$$

we should use $(r/r_0)^c$ instead of r/r_0 in Eq. (10) for such a profile.

The scalings for several moments are shown in Fig. 3. Gathering various slope values, the observational curve of $(q, K(q))$ in the range of $0 \leq q \leq 2$ is indicated in Fig. 4 in cyan. Considering the error for $K(q)$ at each q , the theoretical curve for the multifractal model (Eq. (6)) is fitted to the data. The best fit curve (black curve in Fig. 4) has a multifractal index of $\alpha = 1.63 \pm 0.04$, and the codimension of the mean is $C_1 = 0.373 \pm 0.007$. These values are largely consistent with previous results for atmospheric dissipation fields ($\alpha = 1.35 \pm 0.07$, $C_1 = 0.3 \pm 0.05$ for the horizontal shear of a velocity field (Chigirinskaya et al., 1994); $\alpha = 1.85 \pm 0.05$, $C_1 = 0.59 \pm 0.05$ for vertical kinetic energy flux (Lazarev et al., 1994)).

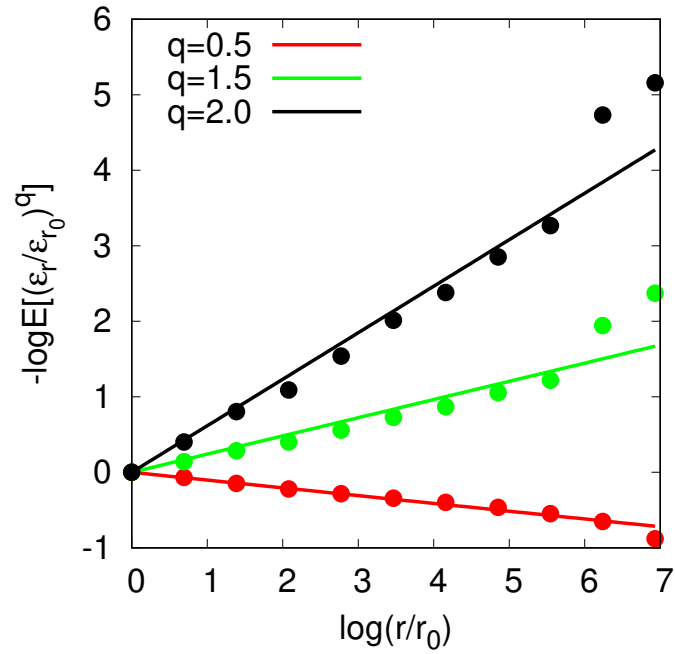


Figure 3. Scale dependency of the moments, $\left(\log(r/r_0), -\log\left\langle(\epsilon_r/\epsilon_{r_0})^{q/c}\right\rangle\right)$, where r_0 is the width of observational bin. The moment scaling exponents are derived as $K(0.5) = -0.103 \pm 0.006$, $K(1.5) = 0.241 \pm 0.036$, $K(2.0) = 0.616 \pm 0.053$.

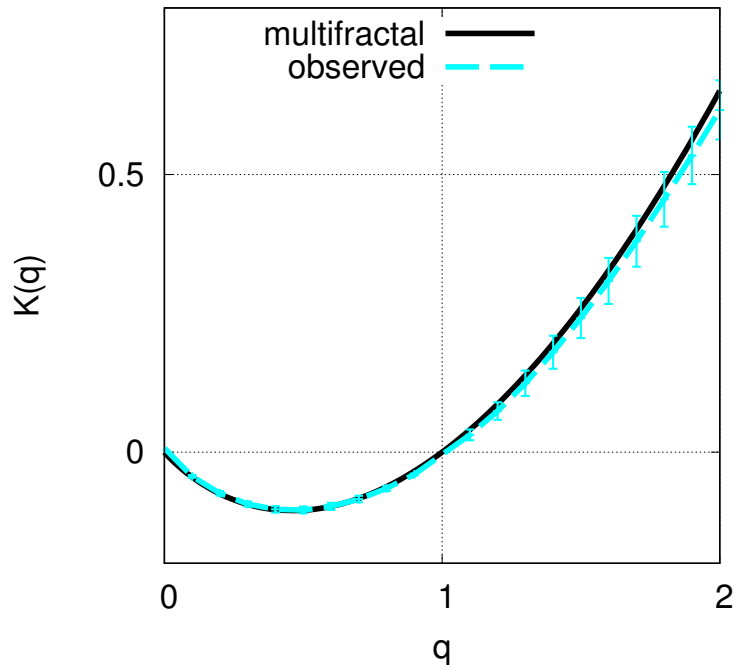


Figure 4. Moment scaling exponent $K(q)$ for observational data (cyan), and the best-fitting multifractal model (black). Each error bar in cyan shows the standard deviation for each $K(q)$.

Figure 5 shows the theoretical curve of extremes for the multifractal model (Eq. (7)) in black and the observational curve,

$$c_{\text{obs}}(\gamma) = -\log_{\lambda} Pr(\epsilon_{r_0}/\epsilon_L > \lambda^{\gamma}), \quad \lambda = L/r_0,$$

in cyan, where $\lambda = 2^8$ is used, which is a typical scale ratio in the data. The two curves appear to be in good agreement up to a slowly varying function of γ . Moreover, as our data have sampling dimension $D_s = \log_{\lambda} N_s \simeq \log 400 / \log(2^8) = 1.08$, the upper bound for q is calculated to be $q_s = 2.85$ (the slope of the navy line in Fig. 5), which justifies the range we set ($0 \leq q \leq 2$).

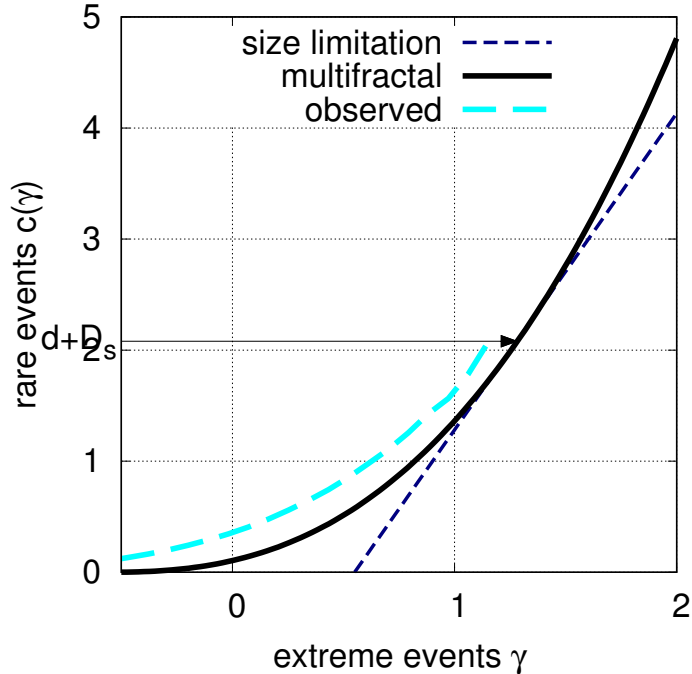


Figure 5. Codimension $c(\gamma)$ of singularities γ for multifractal model (black). The corresponding curve for observation is shown for reference (cyan). Sampling dimension D_s and the limitation for the moment exponent (the slope of the navy line) are also shown.

To demonstrate the appropriateness of the universal multifractal model, the histogram for the logarithm of bin values in observational data is shown in Fig. 6 and compared with samples from multiplicative cascade models, which are detailed in sec. 4.1. Each bin value, ϵ_{r_0} , is normalized by the arithmetic mean, ϵ_L , along the profile it belongs to. The histogram for the logarithm of bin data, $\log_{10} \epsilon_{r_0}/\epsilon_L$, appears to be in good agreement with the histogram of samples generated by the 8-step cascade model with stable Lévy generators (black; $\alpha = 1.63$, $C_1 = 0.373$) and in poor agreement with the histogram generated by the multifractal model with Gaussian generators (red; $\alpha = 2$, $C_1 = 0.399$). In particular, the former reproduces the observed power-law decay at the left tail (Property 1.2.15 of Samorodnitsky and Taqqu, 1994) as

$$\lim_{\gamma \rightarrow \infty} \gamma^\alpha Pr(\epsilon_{r_0}/\epsilon_L < \lambda^{-\gamma}) = \frac{C_1 (\log \lambda)^{1-\alpha}}{\Gamma(2-\alpha)} = 5.28 \times 10^{-2}, \quad \lambda = L/r_0 = 2^8,$$

This implies that if $\epsilon_{r_0}/\epsilon_L$ is small, the probability density function for $\log_\lambda(\epsilon_{r_0}/\epsilon_L)$ is approximated as

$$p(\log_\lambda(\epsilon_{r_0}/\epsilon_L) = -\gamma) \doteq 5.28 \times 10^{-2} \alpha \gamma^{-\alpha-1}. \quad (13)$$

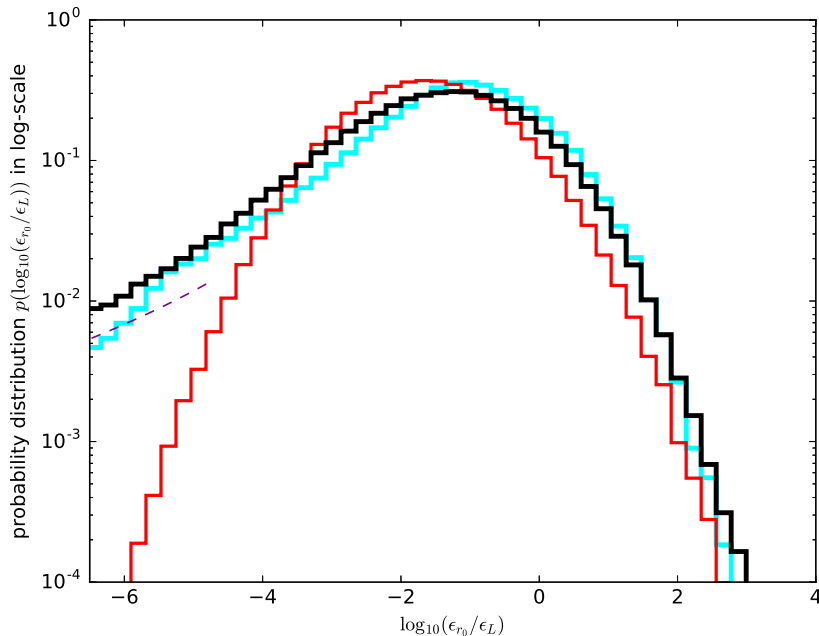


Figure 6. Distribution of the logarithm of observational data normalized for each profile (cyan) and comparison with the statistics of samples generated from multiplicative cascade with Gaussian/stable Lévy generators (red/black). Asymptote for left tail of black curve, Eq. (13), is also shown (purple dashed).

Moreover, in the same manner as the correlation in Yaglom's cascade, it is shown that the observational profiles have a power-law autocorrelation,

$$\langle \epsilon(z)\epsilon(z + \ell) \rangle \propto \ell^{-K(2)} = \ell^{-0.648}, \quad (14)$$

where z is depth. This also explains the discontinuous characteristics observed in the profiles (see Fig. 2(a)).

4 Estimations based on the cascade model

4.1 Multiplicative cascade simulation

To examine the relationship between various statistical quantities derived from observational profiles, we construct a simulation model for the multiplicative cascade by following the procedure described in Schmitt (2003), as shown in Fig. 7. Each building block, Γ_{ik} , is a generator that obeys a left-skewed stable distribution, $S_\alpha(\sigma h^{1/\alpha}, -1, -\widehat{\sigma}_\alpha^\alpha h)$, with $h \equiv \log 2$, $\widehat{\sigma}_\alpha^\alpha \equiv \sigma^\alpha / \cos \frac{\pi}{2}(2 - \alpha) = C_1/(\alpha - 1)$ (e.g., Samorodnitsky and Taqqu, 1994).

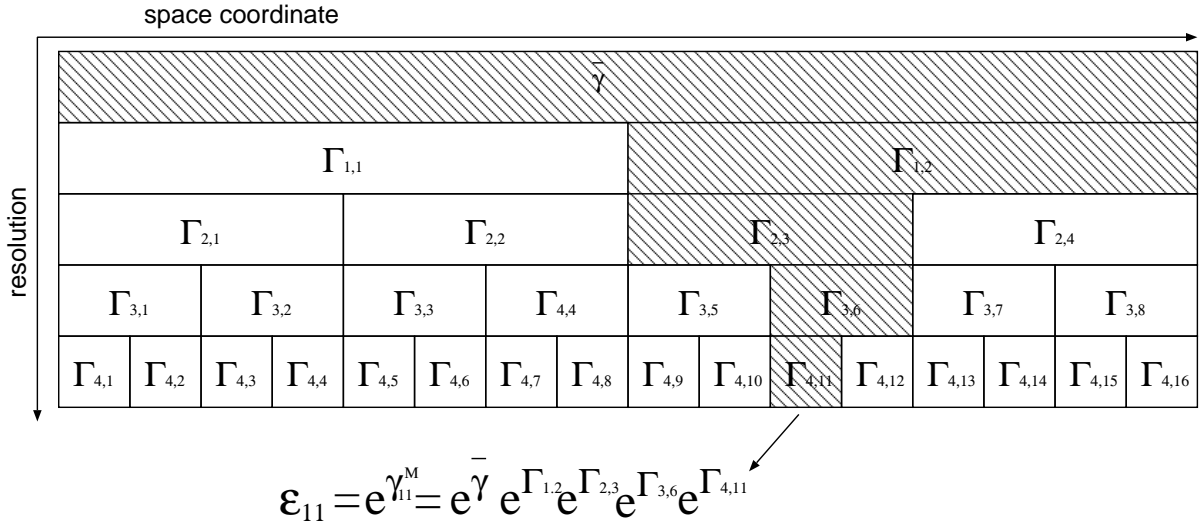


Figure 7. Schematic of the multiplicative cascade model. The energy dissipation rate at z_{11} at resolution $r_4 = L/2^4$ is considered as an example.

Consider a fixed horizontal position. The cascade simulation is performed for variable $X_{i,j}$ with scale index $0 \leq i \leq n$ and spatial index $1 \leq j \leq 2^n$, where $n = \log_2 \frac{L}{r}$.

1. For each spatial index $j = 1, 2, \dots, 2^n$, set $X_{0,j} = 0$.
2. For each scale index $i = 1, \dots, n$, repeat the following steps:
 - For each spatial block $k = 1, 2, \dots, 2^i$, perform the following steps:
 - (a) Generate a random variable, ξ_{ik} , which obeys $S_\alpha(1, -1, 0)$ (Misiorek and Weron, 2012).
 - (b) For each spatial index $j = (k-1) \cdot 2^{n-i} + 1, \dots, k \cdot 2^{n-i}$, downscale X by

$$X_{i,j} = X_{i-1,j} - \widehat{\sigma}_\alpha^\alpha h + \sigma h^{\frac{1}{\alpha}} \xi_{ik}.$$

Using the simulated variable, $X_{n,j}$, the energy dissipation rate at the horizontal position, \mathbf{x} , and the vertical position, $z_j \in [(j-1)r_n, jr_n]$ at resolution $r_n = L/2^n$ is derived as follows:

$$\epsilon_{r_n}(\mathbf{x}, z_j) = \bar{\epsilon}(\mathbf{x}) \exp(X_{n,j}), \quad (15)$$

where $\bar{\epsilon}(\mathbf{x}) = \exp(\bar{\gamma}(\mathbf{x}))$ denotes the energy input rate from an external force at the horizontal position.

An important implication in this formulation is that the arithmetic average of the vertical data points is not necessarily equal to the the energy input rate because the cascade process has a fluctuating nature. In other words, a realization of the vertical average, $2^{-n} \sum_{j=1}^{2^n} \exp(X_{n,j})$, is not always equal to 1, whereas expectation $\mathbb{E} \left[2^{-n} \sum_{j=1}^{2^n} \exp(X_{n,j}) \right] = 1$. Below, we focus

mainly on the relationship between the following three statistical quantities: the arithmetic average over a profile, the geometric average over a profile, and the energy input rate. We perform statistical estimations for these quantities based on the cascade model.

4.2 Arithmetic average vs. geometric average

Oceanographers frequently use the logarithm of ϵ to visualize the dissipation field and compare the corresponding field derived by a parameterization scheme (e.g., Scheifele et al., 2018; Whalen et al., 2015; Waterhouse et al., 2014; Cuypers et al., 2012; Gargett, 1999; Smyth et al., 1997). One reason is that the logarithmic field has a spatially correlated structure, whose shape is relatively easy to recognize, whereas the original field has a highly intermittent structure. The averaging rule of the energy dissipation rate in the logarithmic space is important for such practical purposes. Thus, we examine how the statistics of observational data and their logarithm vary in the realizations of the vertical profile generated by the above cascade model.

We fix a horizontal point, \mathbf{x} , and consider the energy input rate, $\bar{\epsilon} = \bar{\epsilon}(\mathbf{x})$, at this point. According to Eq. (15), the expected values of the arithmetic average, A_a , and the geometric average, A_g , among $m = 2^i$ neighboring points in the n -step cascade given an energy input rate are

$$A_a(2^i; \bar{\epsilon}) = \mathbb{E} \left[2^{-i} \sum_{j=(k-1) \cdot 2^i + 1}^{k \cdot 2^i} \epsilon_{r_n}(z_j) \middle| \bar{\epsilon} \right] = \bar{\epsilon} \mathbb{E} \left[2^{-i} \sum_{j=(k-1) \cdot 2^i + 1}^{k \cdot 2^i} e^{X_{n,j}} \right] = \bar{\epsilon}, \quad (16)$$

$$A_g(2^i; \bar{\epsilon}) = \mathbb{E} \left[\exp \left(2^{-i} \sum_{j=(k-1) \cdot 2^i + 1}^{k \cdot 2^i} \gamma_j \right) \middle| \bar{\epsilon} \right] = \bar{\epsilon} \mathbb{E} \left[\exp \left(2^{-i} \sum_{j=(k-1) \cdot 2^i + 1}^{k \cdot 2^i} X_{n,j} \right) \right], \quad (17)$$

where $\gamma_j = \log \epsilon_{r_n}(z_j)$, $\epsilon_{r_n}(z_j)$ denotes the energy dissipation rate for the observed length scale, r_n , and j denotes the spatial index. Note that the expectation is also taken across all possible segments, $k = 1, 2, \dots, 2^{n-i}$. As the ratio of the expected values of the geometric average to the arithmetic average,

$$\Phi(2^i) \equiv \frac{A_g(2^i; \bar{\epsilon})}{A_a(2^i; \bar{\epsilon})} = \mathbb{E} \left[\exp \left(2^{-i} \sum_{j=(k-1) \cdot 2^i + 1}^{k \cdot 2^i} X_{n,j} \right) \right], \quad (18)$$

is independent of the energy input rate, $\bar{\epsilon}$, we can define an estimator for $\bar{\epsilon}$ as

$$\mathcal{E}_g(2^i) = \frac{1}{\Phi(2^i)} \exp \left(2^{-i} \sum_{j=(k-1) \cdot 2^i + 1}^{k \cdot 2^i} \gamma_j \right). \quad (19)$$

The expected value of $\mathcal{E}_g(2^i)$ is $\bar{\epsilon}$, which implies that the estimator is unbiased. The relative error, η , for the estimator, $\mathcal{E}_g(2^i)$, is

$$\eta(\mathcal{E}_g(2^i)) = \frac{\sqrt{\text{var} \left[\frac{1}{\Phi(2^i)} \exp \left(2^{-i} \sum_{j=(k-1) \cdot 2^i + 1}^{k \cdot 2^i} \gamma_j \right) \middle| \bar{\epsilon} \right]}}{\mathbb{E} \left[\frac{1}{\Phi(2^i)} \exp \left(2^{-i} \sum_{j=(k-1) \cdot 2^i + 1}^{k \cdot 2^i} \gamma_j \right) \middle| \bar{\epsilon} \right]} = \frac{\sqrt{\text{var} \left[\exp \left(2^{-i} \sum_{j=(k-1) \cdot 2^i + 1}^{k \cdot 2^i} X_{n,j} \right) \right]}}{\mathbb{E} \left[\exp \left(2^{-i} \sum_{j=(k-1) \cdot 2^i + 1}^{k \cdot 2^i} X_{n,j} \right) \right]}, \quad (20)$$

while that for the arithmetic average, $\mathcal{E}_a(2^i)$, is

$$\eta(\mathcal{E}_a(2^i)) = \sqrt{\text{var} \left[2^{-i} \sum_{j=(k-1) \cdot 2^i + 1}^{k \cdot 2^i} e^{X_{n,j}} \right]}. \quad (21)$$

We calculate these statistics, $A_a(2^i)$, $A_g(2^i)$, $\eta(\mathcal{E}_a(2^i))$, and $\eta(\mathcal{E}_g(2^i))$, for $i = 0, 1, \dots, n$, using the simulation model for the 10-step ($n = 10$) multiplicative cascade. The result is shown in Fig. 8. It is clear that the relative error for $\mathcal{E}_g(2^i)$ is comparable to that for $\mathcal{E}_a(2^i)$ for any i . For this reason, the geometric average can also be used for estimating the energy input rate, $\bar{\epsilon}$, provided that it is appropriately scaled up using factor $1/\Phi(2^i)$.

Figure 8 shows the following: If the geometric average of 256 neighboring points is considered as an example, the input rate, $\bar{\epsilon}$, is expected to be $1/0.0776 = 12.8$ times larger than the geometric average, as shown by the navy-blue curve at the number of points = 256. However, after rescaling, the geometric average should be almost as accurate as the arithmetic average for estimating the energy input rate, provided that the multiplicative cascade model is accepted.

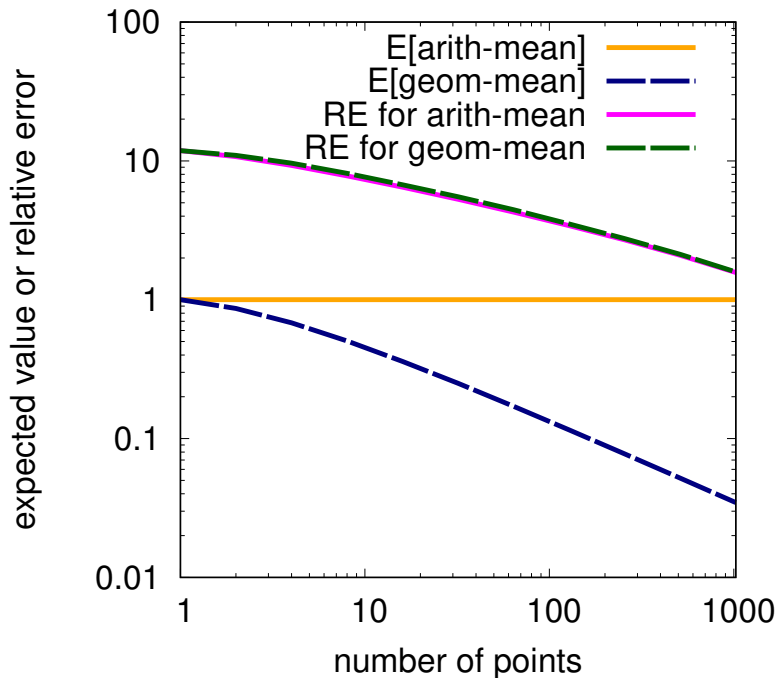


Figure 8. Expected values of arithmetic mean $A_a(m)$ (orange) and geometric mean $A_g(m)$ (navy blue) according to the number of neighboring points, m . The energy input rate, $\bar{\epsilon}$, is fixed at 1. The relative errors for the estimators, $\eta(\mathcal{E}_a(m))$ and $\eta(\mathcal{E}_g(m))$, are also shown (magenta and green, respectively).

4.3 Bayesian estimation of the energy input rate

In this section, we discuss how to estimate the energy input rate by fully utilizing the information obtained from an observational profile. Even though it is primarily indicated by the arithmetic average of vertical data values, as shown in the previous subsection, there still is a requirement for obtaining information regarding the estimation error. For this purpose, we treat the estimation problem as a Bayesian inference, which can be solved by assimilating data into the cascade model in the logarithmic space.

4.3.1 Data assimilation problem

Suppose we have an observed profile, $\gamma^{\text{obs}} \stackrel{\text{def}}{=} \{\gamma_j^{\text{obs}} | j = 1, 2, 3, \dots, 2^n\}$, where $\gamma_j^{\text{obs}} = \log \epsilon_j^{\text{obs}}$ and j is the vertical order of the sequence. We use the cascade described in sec. 4.1 with step size $n = 8$, which generates a profile with $2^8 = 256$ points.

The data assimilation for estimating the logarithm of energy input rate $\bar{\gamma}$ is formulated as a problem of deriving the posterior probability density,

$$p(\bar{\gamma} | \gamma^{\text{obs}}) = \int_{\Gamma} p(\bar{\gamma}, d\Gamma | \gamma^{\text{obs}}) \stackrel{\text{def}}{=} \frac{\sum_{\Gamma} f(\bar{\gamma}, \Gamma)}{\sum_{\bar{\gamma}, \Gamma} f(\bar{\gamma}, \Gamma)}, \quad (22)$$

$$f(\bar{\gamma}, \Gamma) \stackrel{\text{def}}{=} \pi_{\alpha}(\bar{\gamma} - \hat{\gamma}) \left[\prod_{i=1}^n \prod_{k=1}^{2^i} \pi_{\alpha}(\Gamma_{ik} - \Gamma_0) \right] \exp \left(- \sum_{j=1}^{2^n} \frac{(\gamma_j^{\text{obs}} - \mathcal{M}_j(\bar{\gamma}, \Gamma))^2}{2\sigma_{\text{obs}}^2} \right), \quad (23)$$

where \sum_x represents the sum across the ensemble members of x , \mathcal{M}_j is the j -th output of the n -step cascade model, $\hat{\gamma} \stackrel{\text{def}}{=} \log \left(2^{-n} \sum_{j=1}^{2^n} \epsilon_j^{\text{obs}} \right)$, $\Gamma_0 \stackrel{\text{def}}{=} - \frac{\sigma_{\alpha}}{\cos \frac{\pi}{2}(2-\alpha)} h$, $\pi_{\alpha}(\cdot)$ is the probability density function for stable distribution $S_{\alpha}(\sigma h^{1/\alpha}, -1, 0)$, and σ_{obs}^2 is the observational variance. The first two terms on the right hand side of Eq. (23) represent the prior probabilities for $\bar{\gamma}$ and Γ , and the last term represents the likelihood of observation. We set $\sigma_{\text{obs}} = 1.0$ based on a comparison between thermistors and shear probes (Fig. 6 of Goto et al., 2016).

The expected value of $\bar{\epsilon}$ given observation $\epsilon_j^{\text{obs}} = e^{\gamma_j^{\text{obs}}}$, $j = 1, 2, \dots, 2^n$ is calculated as

$$\mathbb{E}[\bar{\epsilon} | \epsilon^{\text{obs}}] \stackrel{\text{def}}{=} \sum_{\bar{\gamma}} e^{\bar{\gamma}} \frac{\sum_{\Gamma} f(\bar{\gamma}, \Gamma)}{\sum_{\bar{\gamma}, \Gamma} f(\bar{\gamma}, \Gamma)}. \quad (24)$$

The solution procedure is detailed in Appendix B.

One possible drawback of this approach is that the moment scaling exponent for the cascade, which was analyzed in the previous section, could be different with and without the consideration of the observational error. Nevertheless, for simplicity, we use the fixed parameter values of $\alpha = 1.63$ and $C_1 = 0.373$ throughout this estimation study.

4.3.2 Identical twin experiment

An identical twin experiment is performed for estimating the energy input rate to confirm the efficacy of the data assimilation scheme. After obtaining pseudo-observations using the cascade model, the estimation problem is solved by first performing

annealed importance sampling (AIS; Neal (2001)), resampling its final state, and subsequently using a Markov chain Monte Carlo method (Metropolis et al., 1953). The procedure for the identical twin experiment is as follows:

1. Create an observational profile from a true input rate.
 - (a) Generate an energy input rate, $\bar{\epsilon}_{\text{true}} = e^{\bar{\gamma}_{\text{true}}}$, randomly.
 - (b) Compute the energy dissipation rates, γ_j^M , $j = 1, 2, \dots, 2^n$ according to the procedure described in sec.4.1.
 - (c) Calculate γ_j^{obs} by adding independent Gaussian noise to γ_j^M .
2. Estimate the conditional probability density of $\bar{\gamma}$ according to Eq. (22) using AIS. For details, see Appendix B.
3. Compare the conditional expectation of $\bar{\epsilon}$ (Eq. (24)) to the true value, $\bar{\epsilon}_{\text{true}}$.

The result of the identical twin experiment is shown in Fig. 9. The conditional expectation divided by the true value, $\mathbb{E}[\bar{\epsilon} | \epsilon^{\text{obs}}] / \bar{\epsilon}_{\text{true}}$, is shown in green, and the arithmetic mean and geometric mean divided by true value are shown in magenta and blue, respectively. The accuracies of the conditional expectation and arithmetic mean are calculated as

$$\mathcal{A}_{\text{est}} = \sqrt{N^{-1} \sum_{n=1}^N \left(\mathbb{E}[\bar{\epsilon} | \epsilon_{(n)}^{\text{obs}}] / \bar{\epsilon}_{(n)}^{\text{true}} - 1 \right)^2}, \quad \mathcal{A}_{\text{arith}} = \sqrt{N^{-1} \sum_{n=1}^N \left(\hat{\epsilon}_{(n)} / \bar{\epsilon}_{(n)}^{\text{true}} - 1 \right)^2}, \quad (25)$$

where n indicates the case number of the experiment. In this identical twin experiment, the accuracy of the conditional expectation, $\mathcal{A}_{\text{est}} = 0.61$, is more than that of the arithmetic mean, $\mathcal{A}_{\text{arith}} = 0.85$. This indicates that data assimilation improves the accuracy of the estimation of the energy input rate. It is important to note that data assimilation also provides the estimation error, which cannot be provided by the arithmetic mean. As an example, error bars are indicated as the 1-st to 99-th percentile in Fig. 9. Here, the x -th percentile represents the value at which the conditional cumulative distribution function points at $x\%$.

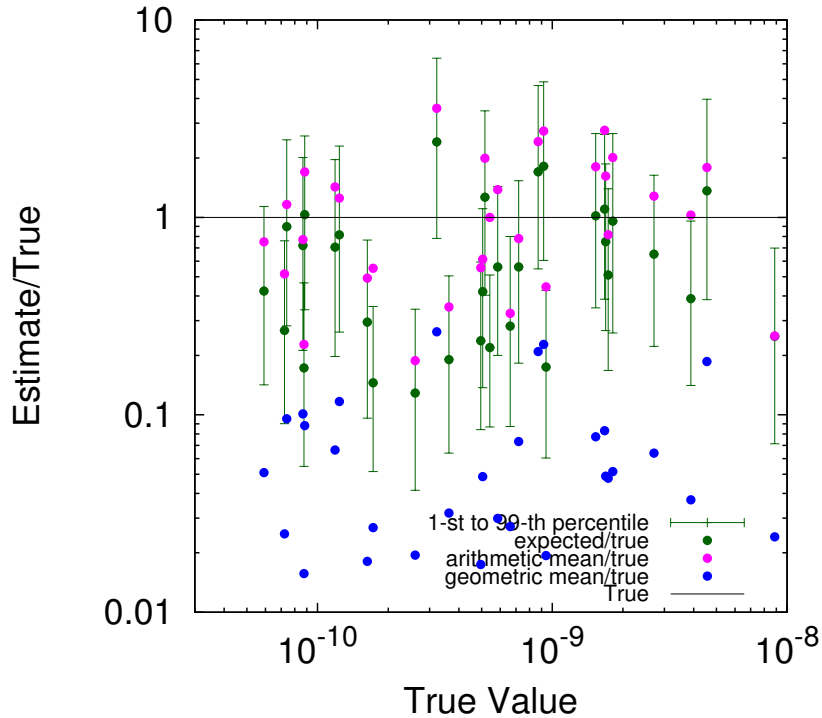


Figure 9. Result of identical twin data assimilation experiments with the 8-step cascade model (32 independent cases). Conditional expectation divided by true value, $\mathbb{E}[\bar{\epsilon}|\epsilon^{\text{obs}}]/\bar{\epsilon}_{\text{true}}$, is shown (green) along with the 1-st to 99-th percentile. Arithmetic mean and geometric mean divided by true value are also shown for comparison (magenta and blue, respectively).

4.3.3 Real data experiment

A data assimilation experiment is performed using the same procedure as the identical twin experiment, except that real profile data are used instead of pseudo-observations. Note that we use the generators with $C_1 = 0.373c$ if the profile has uneven observational spacing to be consistent with the treatment in Eq. (11), where c is defined in Eq. (12).

The overview of the result is shown in Fig. 10 as a horizontal distribution of the estimated energy input rate, along with the arithmetic mean across the profile. The estimation also provides the a posterior probability density for the estimation of $\bar{\gamma}$, which varies from profile to profile, as shown in the histograms in Fig. 11. To improve visibility, the arithmetic mean, the geometric mean, and the estimated value with the 1-st and 99-th percentiles are shown along several geographical sections in Figs. 12, 13, and 14. In most cases, the arithmetic mean lies within the range of the two percentiles, whereas the geometric mean is one tenth or less than the estimated value. In addition, it is suggested that extremely large values of the arithmetic mean, which occasionally occur owing to intermittency, can be suppressed in the estimation of the energy input rate (see Fig. 12 for typical examples).

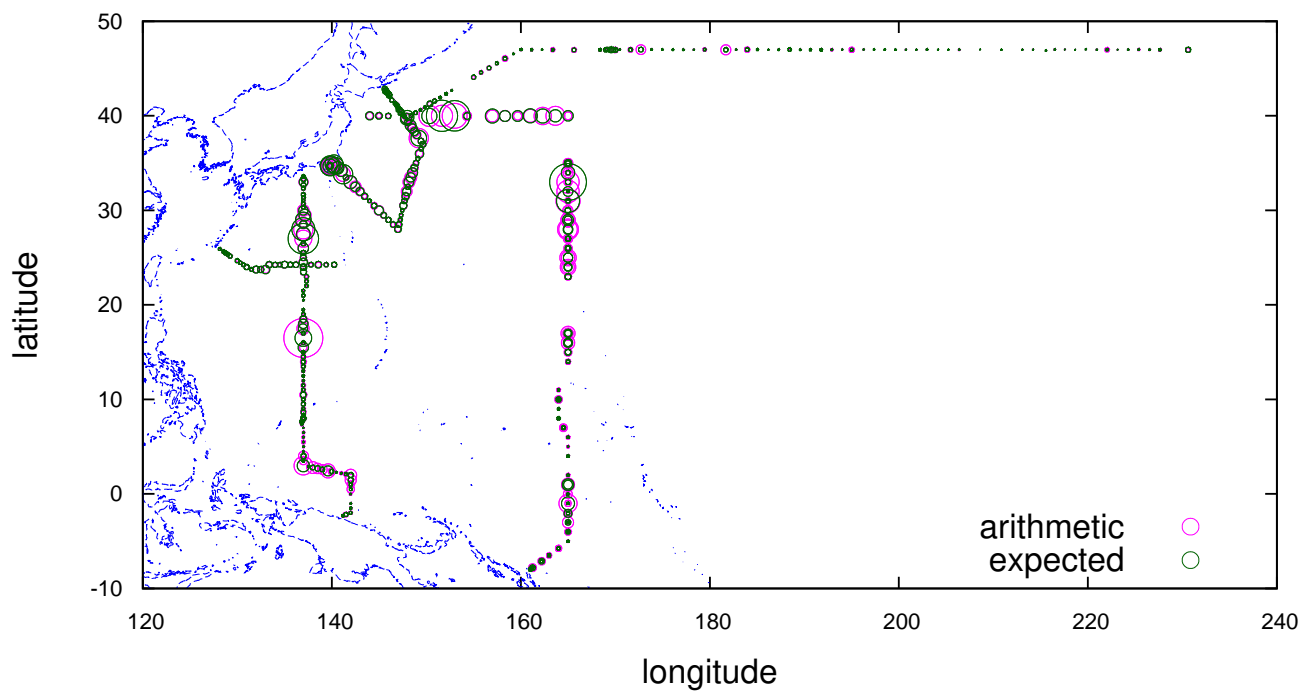


Figure 10. Horizontal distribution of estimated energy input rate (green) and arithmetic mean (magenta). The area of each circle is proportional to the magnitude of the corresponding value in linear scale. The units of longitude and latitude are $^{\circ}$ E and $^{\circ}$ N, respectively.

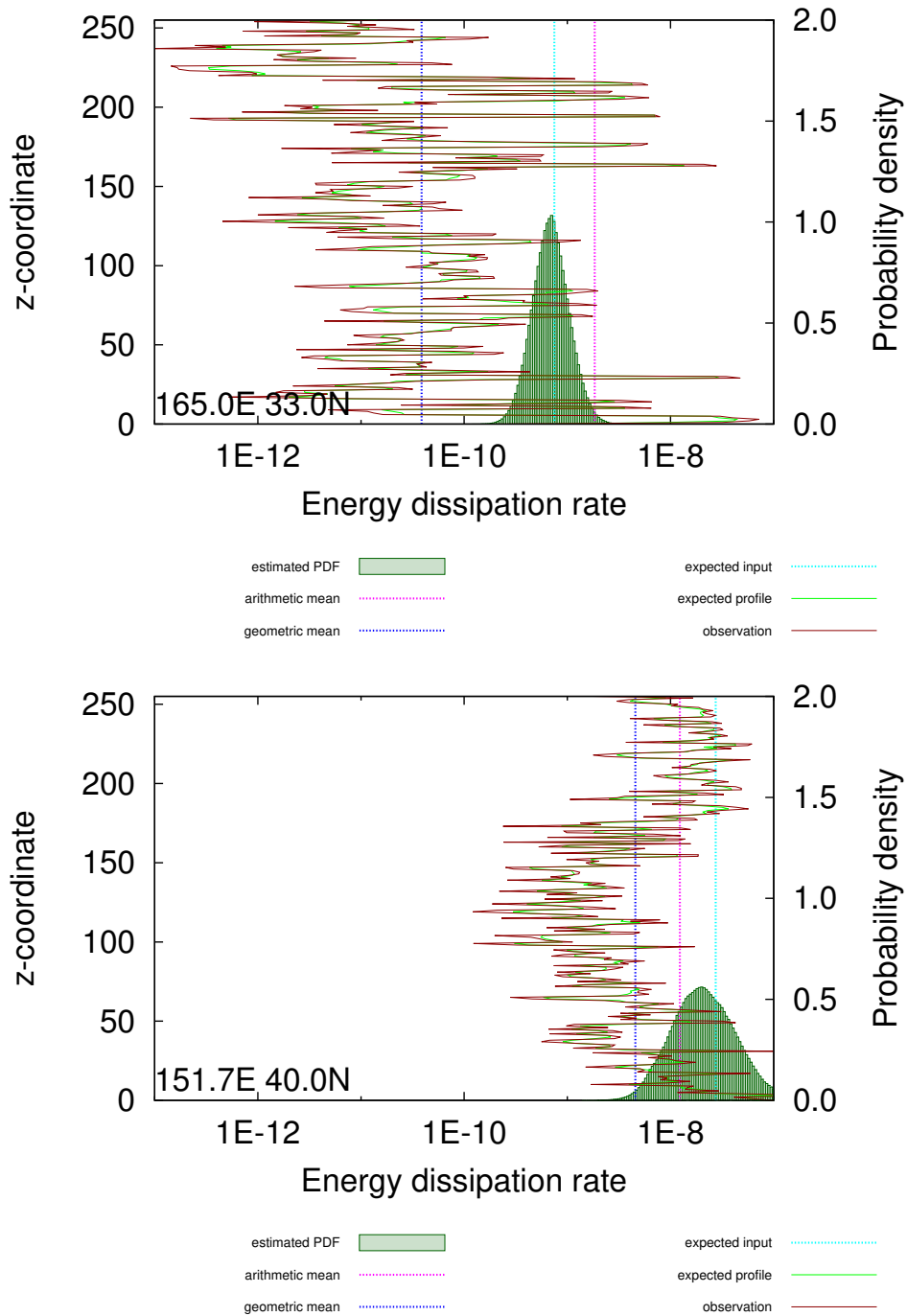


Figure 11. The posterior distributions of the energy input rate (histogram in green) given a vertical profile of the energy dissipation rate (dark red). The vertical line in cyan represents the expected value of the energy input rate. The vertical lines in blue and magenta represent the geometric mean and arithmetic mean over the observed profile, respectively.

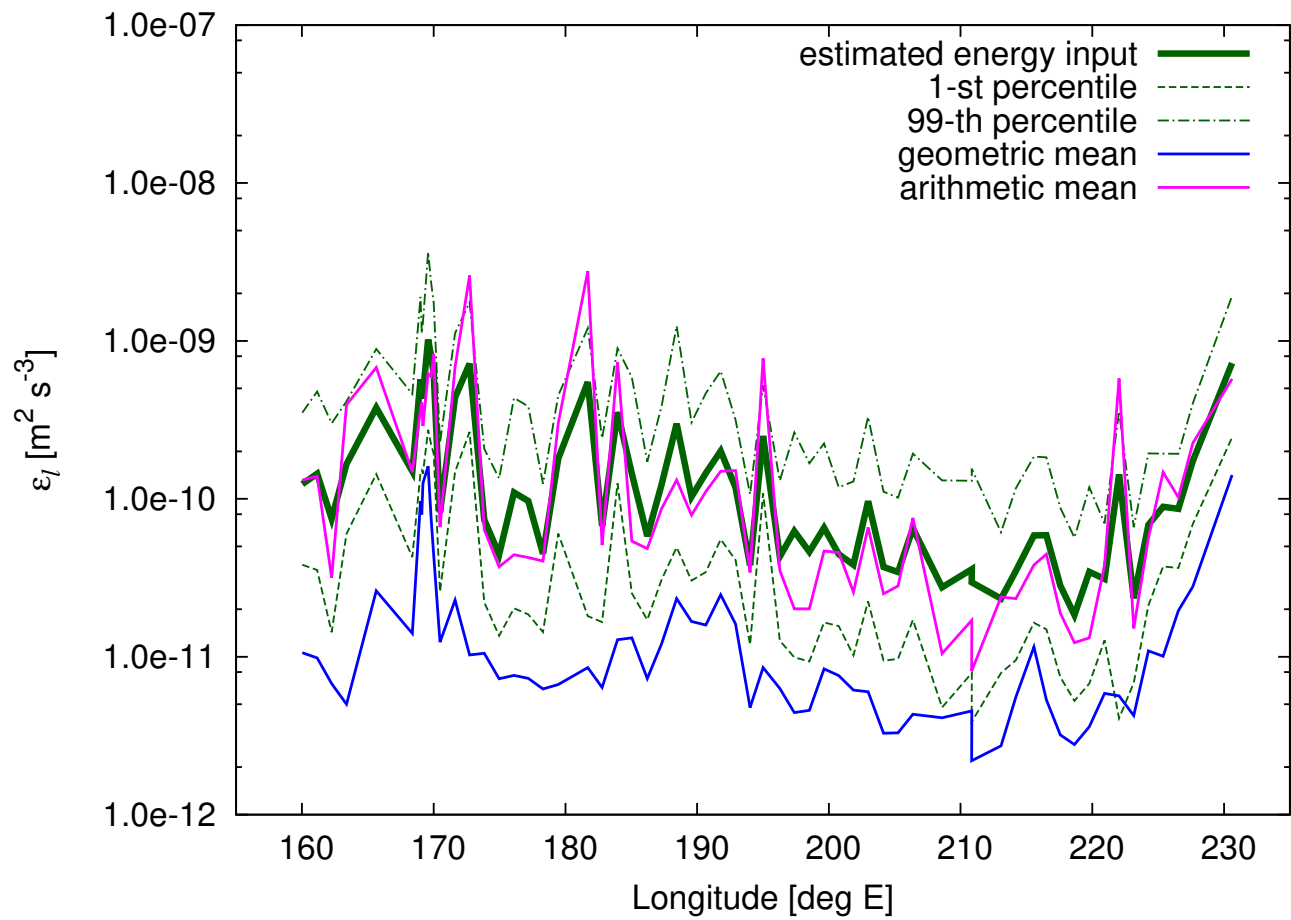


Figure 12. Horizontal distribution of estimated energy input rate (green), arithmetic mean (magenta), and geometric mean (blue) along 47°N . The 1-st (green dash) and 99-th (green dash-dot) percentiles for estimation are also shown. The units of longitude is $^\circ\text{E}$.

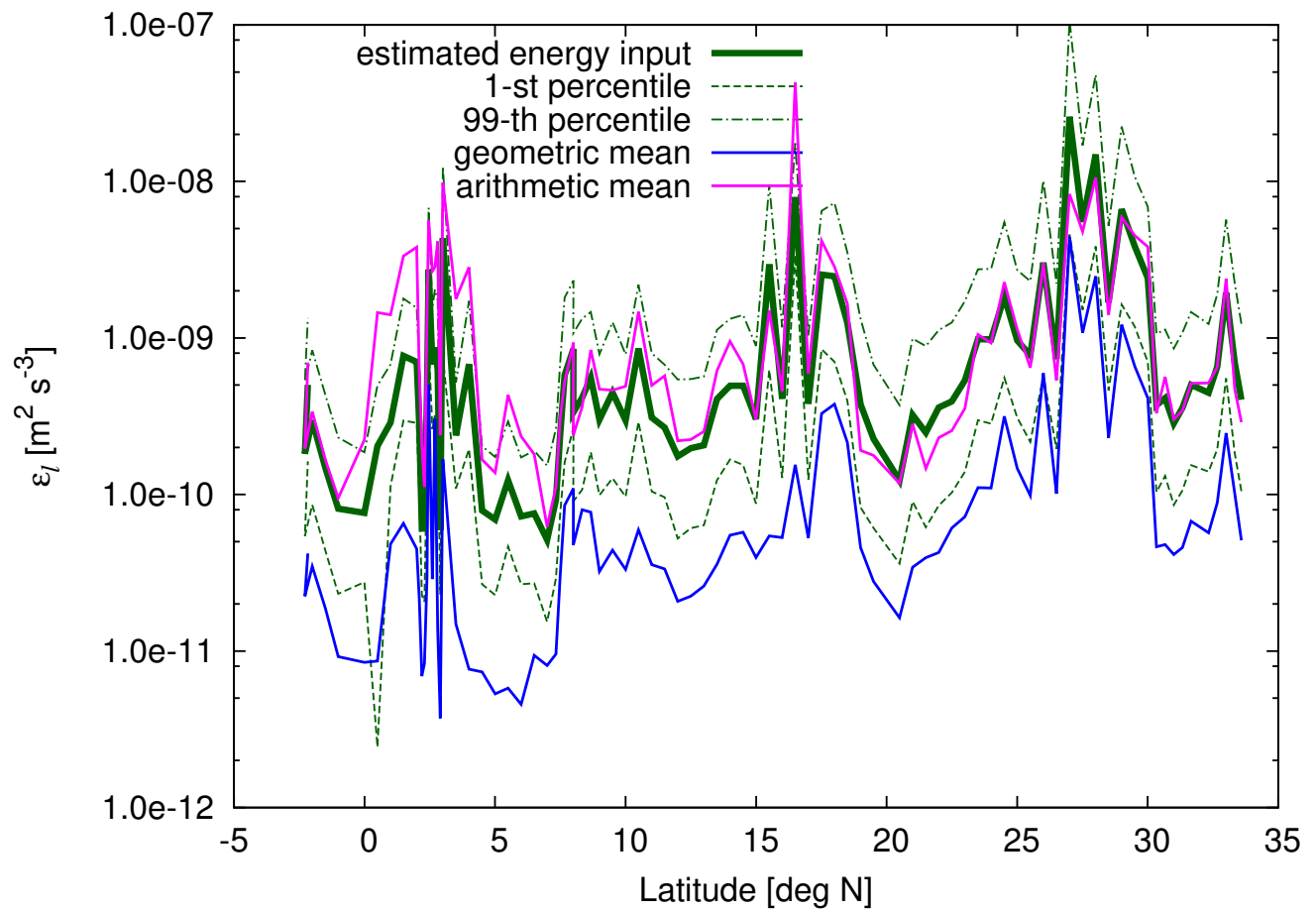


Figure 13. Horizontal distribution of estimated energy input rate (green), arithmetic mean (magenta), and geometric mean (blue) along 137°E . The 1-st (green dash) and 99-th (green dash-dot) percentiles for estimation are also shown. The units of latitude is $^\circ\text{N}$.

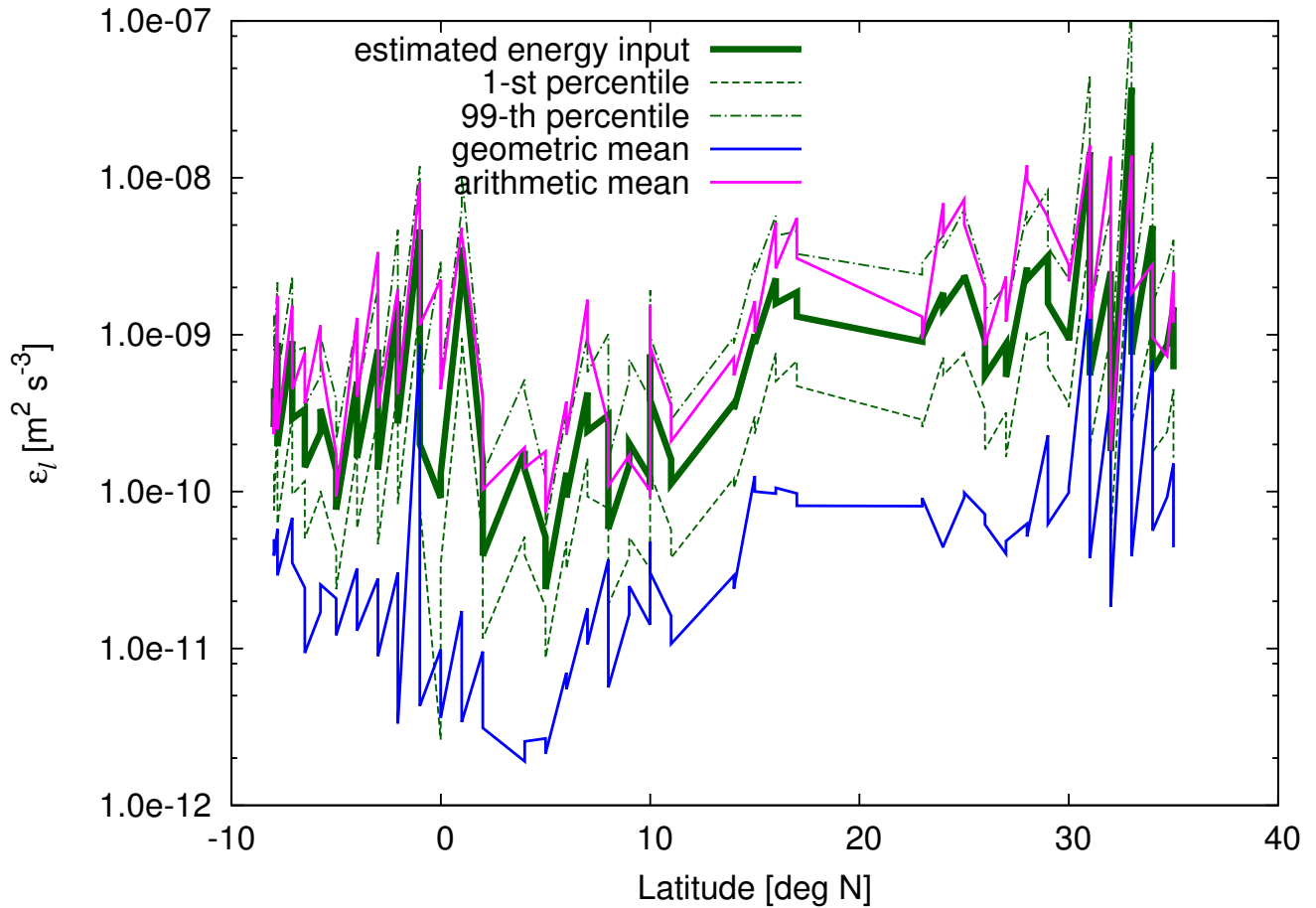


Figure 14. Horizontal distribution of estimated energy input rate (green), arithmetic mean (magenta), and geometric mean (blue) along 165°E . The 1-st (green dash) and 99-th (green dash-dot) percentiles for estimation are also shown. The units of latitude is $^\circ\text{N}$.

5 Conclusions

We have analyzed the observed data obtained from oceanic turbulence and shown that the vertical sequences of depth-averaged energy dissipation rates have an intermittent structure that obeys a scaling law. Furthermore, we have proposed a method of estimating the energy input rate from given observations by utilizing that property.

1. For scaling in the observed profiles, the statistical property of our data is consistent with the universal multifractal model, which has a moment scaling exponent of $K(q) = \frac{C_1}{\alpha-1}(q^\alpha - q)$ with a multifractal index of $\alpha = 1.63$ and the codimension of the mean as $C_1 = 0.373$. This result elucidates the universality inherent in the oceanic turbulence data.
2. These statistics are used to determine the averaging rule of the energy dissipation rates in the logarithmic space, which has been conventionally used for visualizing the oceanic dissipation field. In addition to the arithmetic average of vertical data points, the geometric average can be used for estimating the energy input rate if it is appropriately scaled up by a factor that depends on the number of averaging points.
3. The energy input rate and its uncertainty can be estimated by assimilating vertical profile data into the cascade model. The estimate acts as an alternative to the arithmetic average over a vertical data sequence. We have used an efficient sampling technique (AIS) as the solver and shown that the application of this inference to real observational data provides more information, i.e., the posterior probability distribution, compared to the arithmetic average alone.
4. Thus, we have found an answer to the question: “how can one estimate energy input rate from the vertical profile data of the energy dissipation rate?” By analyzing the intermittency in the observed data, we can construct a multiplicative cascade model based on the universal multifractal formalism, which can reproduce the statistics of the data. Then, the energy input rate is estimated by assimilating the observed data into the cascade model.
5. Even though we have used a discrete cascade model for simplicity and computational viability, we can extend it to a continuous cascade (e.g., Schmitt and Marsan, 2001), which may improve the estimation accuracy at the cost of computational burden.

Data availability. The ocean turbulence dataset is under preparation for public release by the Atmosphere and Ocean Research Institute, University of Tokyo.

Appendix A: Principle for the estimation of turbulent energy dissipation rate ϵ from fast-response thermistor measurements

ϵ is estimated from the spectra of temperature vertical gradient $\partial T'/\partial z$ using fast-response thermistor FP07 measurements, with a time constant of approximately 7×10^{-3} s (Fig. A1). The Fourier-transformed observed wavenumber temperature gradient spectrum (blue curve) is numerically integrated between the lowest wavenumber and the highest wavenumber at which the spectrum amplitude is more than 1.5 times the noise spectrum (light-blue curve), which is inherent in the instrument, and thermal dissipation rate χ is obtained ($= 6\kappa_T \overline{\left(\frac{\partial T'}{\partial z}\right)^2}$, κ_T is the molecular thermal diffusivity). ϵ is estimated by detecting wavenumber k_P at the peak of the temperature gradient spectrum to yield the Batchelor wavenumber, $k_B (= \left(\frac{\epsilon}{\nu\kappa_T^2}\right)^{\frac{1}{4}}/2\pi)$ (Batchelor, 1959), as $k_B = \sqrt{6q_K}k_P$, at which molecular thermal diffusion begins to work. This peak is detected by fitting the

theoretically derived universal temperature gradient spectrum, (Kraichnan, 1968) $S_{\text{theoretical}}$ (red curve) with the form given in Roget et al. (2006), to the observed spectrum using the maximum likelihood method developed by Ruddick et al. (2000) with the parameters proposed by Peterson and Fer (2014).

$$S_{\text{theoretical}}(k; k_B) = \frac{\chi \sqrt{q_K}}{\kappa_T k_B} y_k^2 \frac{\exp(-\sqrt{6} y_k)}{y_k},$$

where $y_k = \sqrt{q_K} k / k_B$ and q_K is the Kraichnan constant. q_K has been estimated as $q_K = 3.4 - 7.9$ (3.41: Antonia and Orlandi (2003); 5.26 ± 0.25 : Bogucki et al. (1997, 2012), 7.9 ± 2.5 : Sanchez et al. (2011)). We use a fixed value of $q_K = 5.26$, which was introduced in Bogucki et al. (1997, 2012). The Kraichnan spectrum is the modified version of the Batchelor (1959) spectrum considering the intermittency of strain fields. See Goto et al. (2016, 2018) for other detailed estimation procedures.

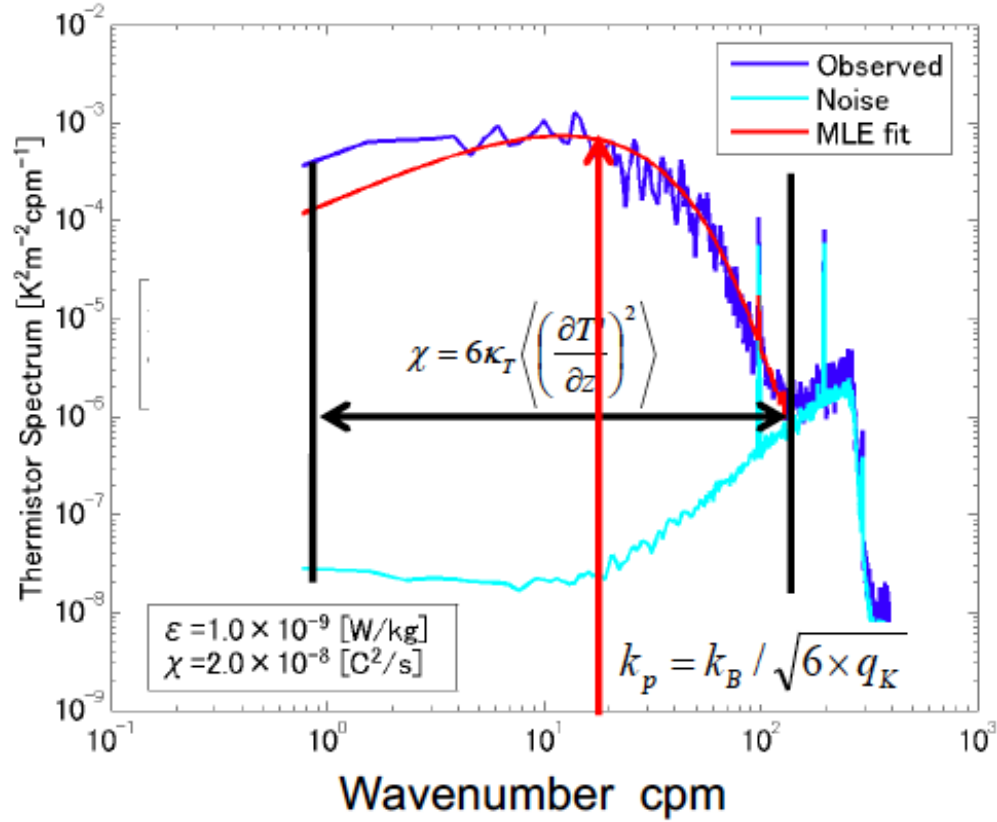


Figure A1. Example of observational wavenumber temperature gradient spectrum (blue curve), noise spectrum (light blue), and fitted theoretical spectrum (red) to detect the wavenumber at spectrum peak k_P to yield Batchelor wavenumber k_B given ϵ .

Appendix B: Solution procedure for data assimilation problem

The data assimilation problem is solved using annealed importance sampling (AIS; Neal (2001)), followed by the Markov chain Monte Carlo (MCMC; Metropolis et al. (1953)) method after resampling. The procedure is as follows:

For each intermediate state, $k = 0, 1, \dots, K$, in AIS, the posterior probability density, p_k , and the corresponding unnormalized probability density, f_k , are defined as

$$p_k(x) \stackrel{\text{def}}{=} f_k(x) / \tilde{Z}_k, \quad (\text{B1})$$

$$f_k(x) \stackrel{\text{def}}{=} f_{\text{bg}}(x) f_{\text{obs}}(x)^{k/K}, \quad (\text{B2})$$

where $x \stackrel{\text{def}}{=} \{\bar{\gamma}, \Gamma_{ik} | 1 \leq i \leq n; 1 \leq k \leq 2^i\}$ and

$$f_{\text{bg}}(x) \stackrel{\text{def}}{=} \pi_\alpha(\bar{\gamma} - \hat{\gamma}) \prod_{i=1}^n \prod_{k=1}^{2^i} \pi_\alpha(\Gamma_{ik} - \Gamma_0), \quad (\text{B3})$$

$$f_{\text{obs}}(x) \stackrel{\text{def}}{=} \exp \left(- \sum_{j=1}^{2^n} \frac{(\gamma_j^{\text{obs}} - \mathcal{M}_j(\bar{\gamma}, \Gamma))^2}{2\sigma_{\text{obs}}^2} \right). \quad (\text{B4})$$

The algorithm for AIS is shown in Algorithm 1 and that for the subsequent MCMC method in Algorithm 2. The transition matrix under the unnormalized probability density, $f_k(\cdot)$, is denoted as $T_k(x \rightarrow x') = T_k(x'|x)$. We use $I = 2560$ particles with $K = 8000$ annealing steps for AIS and $J = 30000$ MCMC steps after resampling.

Algorithm 1 Annealed Importance Sampling

for $1 \leq i \leq I$ **do**

$x_0^{(i)} \leftarrow$ sample from $p_0(\cdot) = f_0(\cdot)$

$w^{(i)} \leftarrow 1$

for $1 \leq k \leq K$ **do**

$x_k^{(i)} \leftarrow$ sample from $T_k(\cdot | x_{k-1}^{(i)})$

$w^{(i)} \leftarrow w^{(i)} \frac{f_k(x_k^{(i)})}{f_{k-1}(x_k^{(i)})}$

end for

$x^{(i)} \leftarrow x_K^{(i)}$

end for

$\tilde{Z} \leftarrow (1/I) \sum_{i=1}^I w^{(i)}$

for $1 \leq i \leq I$ **do**

$w^{(i)} \leftarrow w^{(i)} / \tilde{Z}$

end for

return $\tilde{Z}, \{x^{(i)}\}, \{w^{(i)}\}$

Algorithm 2 Markov chain Monte Carlo method from resampled initial condition

```
for  $1 \leq i \leq I$  do  
   $x_0^{(i)} \leftarrow$  resample from  $\{x^{(i)}\}$  according to weight  $\{w^{(i)}\}$   
  for  $1 \leq j \leq J$  do  
     $x_j^{(i)} \leftarrow$  sample from  $T_K(\cdot | x_{j-1}^{(i)})$   
  end for  
end for  
  
return  $\{x_j^{(i)}\}$ 
```

Author contributions. SM and SO posed the main problem. IY compiled the observational data.

IY, SK, SM, and SO helped formulate the hypothesis. NS proposed the method, performed the statistical analyses, and prepared the manuscript with contributions from all co-authors.

Competing interests. The authors declare that they have no competing interests.

Acknowledgements. The authors are grateful to the reviewers for their valuable comments and suggestions, which helped us improve the manuscript significantly. The helpful comments from Yutaka Yoshikawa (Kyoto University) are appreciated. This work was partially supported by Grant-in-Aid for Scientific Research on Innovative Areas (MEXT KAKENHI-JP15H05817/JP15H05819). We also thank the members of the project for their valuable discussions on the concept and method. We would like to thank Editage for English language editing. All numerical simulations were performed on the JAMSTEC Data Analyzer (DA) system.

References

- Antonia, R. and Orlandi, P.: On the Batchelor constant in decaying isotropic turbulence, *Physics of Fluids*, 15, 2084–2086, 2003.
- Batchelor, G. K.: Small-scale variation of convected quantities like temperature in turbulent fluid Part 1. General discussion and the case of small conductivity, *J. Fluid Mech.*, 5, 113–133, <https://doi.org/10.1017/S002211205900009X>, 1959.
- Benzi, R., Paladin, G., Parisi, G., and Vulpiani, A.: On the multifractal nature of fully developed turbulence and chaotic systems, *Journal of Physics A: Mathematical and General*, 17, 3521, 1984.
- Bogucki, D., Domaradzki, J. A., and Yeung, P.: Direct numerical simulations of passive scalars with $Pr > 1$ advected by turbulent flow, *Journal of Fluid Mechanics*, 343, 111–130, 1997.
- Bogucki, D., Luo, H., and Domaradzki, J.: Experimental evidence of the Kraichnan scalar spectrum at high Reynolds numbers, *Journal of Physical Oceanography*, 42, 1717–1728, 2012.
- Chigirinskaya, Y., Schertzer, D., Lovejoy, S., Lazarev, A., and Ordanovich, A.: Unified multifractal atmospheric dynamics tested in the tropics: part I, horizontal scaling and self criticality, *Nonlinear Processes in Geophysics*, 1, 105–114, <https://doi.org/10.5194/npg-1-105-1994>, <https://www.nonlin-processes-geophys.net/1/105/1994/>, 1994.
- Cuyppers, Y., Bouruet-Aubertot, P., Marec, C., and Fuda, J.-L.: Characterization of turbulence from a fine-scale parameterization and microstructure measurements in the Mediterranean Sea during the BOUM experiment, *Biogeosciences*, 9, 3131–3149, <https://doi.org/10.5194/bg-9-3131-2012>, <https://www.biogeosciences.net/9/3131/2012/>, 2012.
- Frisch, U., Sulem, P.-L., and Nelkin, M.: A simple dynamical model of intermittent fully developed turbulence, *Journal of Fluid Mechanics*, 87, 719–736, 1978.
- Gargett, A. E.: Velcro Measurement of Turbulence Kinetic Energy Dissipation Rate ϵ , *Journal of Atmospheric and Oceanic Technology*, 16, 1973–1993, 1999.
- Gires, A., Tchiguirinskaia, I., Schertzer, D., and Lovejoy, S.: Development and analysis of a simple model to represent the zero rainfall in a universal multifractal framework, *Nonlinear Processes in Geophysics*, 20, 343–356, 2013.
- Goto, Y., Yasuda, I., and Nagasawa, M.: Turbulence Estimation Using Fast-Response Thermistors Attached to a Free-Fall Vertical Microstructure Profiler, *Journal of Atmospheric and Oceanic Technology*, 33, 2065–2078, <https://doi.org/10.1175/JTECH-D-15-0220.1>, 2016.
- Goto, Y., Yasuda, I., and Nagasawa, M.: Comparison of Turbulence Intensity from CTD-Attached and Free-Fall Microstructure Profilers, *Journal of Atmospheric and Oceanic Technology*, 35, 147–162, <https://doi.org/10.1175/JTECH-D-17-0069.1>, 2018.
- Gregg, M., Cox, C., and Hacker, P.: Vertical Microstructure Measurements in the Central North Pacific, *Journal of Physical Oceanography*, 3, 458–469, 1973.
- Gurvich, A. and Zubkovskii, S.: On experimental estimate of the fluctuations of turbulent energy dissipation, *Izv. Akad. Nauk SSSR, Ser. Geofiz.*, 12, 1856, 1963.
- Kolmogorov, A. N.: The local structure of turbulence in incompressible viscous fluid for very large Reynolds numbers, *Cr Acad. Sci. URSS*, 30, 301–305, 1941.
- Kolmogorov, A. N.: A refinement of previous hypotheses concerning the local structure of turbulence in a viscous incompressible fluid at high Reynolds number, *Journal of Fluid Mechanics*, 13, 82–85, 1962.
- Kraichnan, R. H.: Small-scale structure of a scalar field convected by turbulence, *The Physics of Fluids*, 11, 945–953, 1968.
- Landau, L. D. and Lifshitz, E. M.: *Fluid mechanics*, Fluid Mechanics. Second Edition. 1987. Pergamon, Oxford, 1987.

- Lazarev, A., Schertzer, D., Lovejoy, S., and Chigirinskaya, Y.: Unified multifractal atmospheric dynamics tested in the tropics: part II, vertical scaling and generalized scale invariance, *Nonlinear Processes in Geophysics*, 1, 115–123, <https://doi.org/10.5194/npg-1-115-1994>, <https://www.nonlin-processes-geophys.net/1/115/1994/>, 1994.
- Lovejoy, S. and Schertzer, D.: *The Weather and Climate: Emergent Laws and Multifractal Cascades*, Cambridge University Press, 2013.
- Meneveau, C. and Sreenivasan, K.: Simple multifractal cascade model for fully developed turbulence, *Physical review letters*, 59, 1424, 1987.
- Metropolis, N., Rosenbluth, A. W., Rosenbluth, M. N., Teller, A. H., and Teller, E.: Equation of State Calculations by Fast Computing Machines, *The Journal of Chemical Physics*, 21, 1087–1092, <https://doi.org/10.1063/1.1699114>, <https://doi.org/10.1063/1.1699114>, 1953.
- Misiorek, A. and Weron, R.: Heavy-Tailed Distributions in VaR Calculations, pp. 1025–1059, Springer Berlin Heidelberg, Berlin, Heidelberg, 2012.
- Monin, A. S. and Yaglom, A. M.: *Statistical fluid mechanics, volume II: mechanics of turbulence*, vol. 2, chap. 8, Courier Corporation, 2013.
- Munk, W. and Wunsch, C.: Abyssal recipes II: Energetics of tidal and wind mixing, *Deep Sea Research Part I: Oceanographic Research Papers*, 45, 1977–2010, 1998.
- Neal, R. M.: Annealed importance sampling, *Statistics and computing*, 11, 125–139, 2001.
- Parisi, G. and Frish, U.: A multifractal model of intermittency, p. 111–114, Elsevier North Holland, New-York, 1985.
- Peterson, A. K. and Fer, I.: Dissipation measurements using temperature microstructure from an underwater glider, *Methods in Oceanography*, 10, 44–69, 2014.
- Pond, S. and Stewart, R. W.: Measurement of statistical characteristics of small-scale turbulence, *Izv. Akad. Nauk SSSR, Ser. Geofiz*, 1, 914, 1965.
- Pope, S. B.: *Turbulent flows*, Cambridge university press, 2000.
- Richardson, L. F.: *Weather Prediction by Numerical Process*, Cambridge University, Cambridge, 1922.
- Roget, E., Lozovatsky, I., Sanchez, X., and Figueroa, M.: Microstructure measurements in natural waters: Methodology and applications, *Progress in Oceanography*, 70, 126–148, 2006.
- Ruddick, B., Anis, A., and Thompson, K.: Maximum Likelihood Spectral Fitting: The Batchelor Spectrum, *Journal of Atmospheric and Oceanic Technology*, 17, 1541–1555, 2000.
- Samorodnitsky, G. and Taqqu, M. S.: *Non-Gaussian Stable Processes: Stochastic Models with Infinite Variance*, Chapman and Hall, London, 1994.
- Sanchez, X., Roget, E., Planella, J., and Forcat, F.: Small-scale spectrum of a scalar field in water: the Batchelor and Kraichnan models, *Journal of Physical Oceanography*, 41, 2155–2167, 2011.
- Scheifele, B., Waterman, S., Merkelbach, L., and Carpenter, J. R.: Measuring the Dissipation Rate of Turbulent Kinetic Energy in Strongly Stratified, Low-Energy Environments: A Case Study From the Arctic Ocean, *Journal of Geophysical Research: Oceans*, 123, 5459–5480, <https://doi.org/10.1029/2017JC013731>, <https://agupubs.onlinelibrary.wiley.com/doi/abs/10.1029/2017JC013731>, 2018.
- Schertzer, D. and Lovejoy, S.: Elliptical turbulence in the atmosphere, in: *Symposium on Turbulent Shear Flows*, 4 th, Karlsruhe, West Germany, p. 11, 1984.
- Schertzer, D. and Lovejoy, S.: Physical modelling and analysis of rain and clouds by anisotropic scaling and multiplicative processes, *J. Geophys. Res.*, 92, 9693–9714, 1987.
- Schertzer, D. and Lovejoy, S.: Universal multifractals do exist!, *J. Appl. Meteorol.*, 36, 1296–1303, 1997.
- Schmitt, F. and Marsan, D.: Stochastic equations generating continuous multiplicative cascades, *The European Physical Journal B-Condensed Matter and Complex Systems*, 20, 3–6, 2001.

- Schmitt, F. G.: Modeling of Turbulent Intermittency: Multifractal Stochastic Processes and Their Simulation, in: Handbook of scaling methods in aquatic ecology: measurement, analysis, simulation, edited by Seuront, L. and Strutton, P. G., chap. 29, pp. 453–468, CRC Press, 2003.
- Schmitt, F. G. and Huang, Y.: Homogeneous turbulence and intermittency, pp. 12–40, Cambridge University Press, <https://doi.org/10.1017/CBO9781107705548.003>, 2016.
- She, Z.-S. and Leveque, E.: Universal scaling laws in fully developed turbulence, *Physical review letters*, 72, 336, 1994.
- Smyth, W. D., Zavialov, P. O., and Moum, J. N.: Decay of Turbulence in the Upper Ocean following Sudden Isolation from Surface Forcing, *Journal of Physical Oceanography*, 27, 810–822, 1997.
- Waterhouse, A. and McKinnon, J.: Datasets obtained from ocean microstructure profilers, <https://microstructure.ucsd.edu>, 2014.
- Waterhouse, A. F., MacKinnon, J. A., Nash, J. D., Alford, M. H., Kunze, E., Simmons, H. L., Polzin, K. L., St. Laurent, L. C., Sun, O. M., Pinkel, R., Talley, L. D., Whalen, C. B., Huussen, T. N., Carter, G. S., Fer, I., Waterman, S., Naveira Garabato, A. C., Sanford, T. B., and Lee, C. M.: Global Patterns of Diapycnal Mixing from Measurements of the Turbulent Dissipation Rate, *Journal of Physical Oceanography*, 44, 1854–1872, <https://doi.org/10.1175/JPO-D-13-0104.1>, <https://doi.org/10.1175/JPO-D-13-0104.1>, 2014.
- Whalen, C. B., MacKinnon, J. A., Talley, L. D., and Waterhouse, A. F.: Estimating the Mean Diapycnal Mixing Using a Finescale Strain Parameterization, *Journal of Physical Oceanography*, 45, 1174–1188, <https://doi.org/10.1175/JPO-D-14-0167.1>, <https://doi.org/10.1175/JPO-D-14-0167.1>, 2015.
- Yaglom, A. M.: The influence of fluctuations in energy dissipation on the shape of turbulent characteristics in the inertial interval, *Sov. Phys. Dokl.*, 11, 1966.